ReveaLLAGN 0: First Look at JWST MIRI Data of Sombrero and NGC 1052

Kameron Goold[1], Anil Seth[1], Mallory Molina[1,2], David Ohlson[1], Jessie C. Runnoe[2], Torsten Böker[3],
Timothy A. Davis[4], Antoine Dumont[5], Michael Eracleous[6], Juan Antonio Fernández-Ontiveros[7,8], Elena Gallo[9],
Andy D. Goulding[10], Jenny E. Greene[10], Luis C. Ho[11,12], Sera B. Markoff[13], Nadine Neumayer[5],
Richard M. Plotkin[14,15], Almudena Prieto[16,17,18], Shobita Satyapal[19], Glenn van de Ven[20], Jonelle L. Walsh[21],
Feng Yuan[22], Anja Feldmeier-Krause[5], Kayhan Gültekin[9], Sebastian Hönig[23], Allison Kirkpatrick[24],
Nora Lützgendorf[3], Amy E. Reines[25], Jay Strader[26], Jonathan R. Trump[27], and Karina T. Voggel[28]

[1] Department of Physics & Astronomy, University of Utah, James Fletcher Building, 115 1400 E, Salt Lake City, UT 84112, USA
[2] Department of Physics & Astronomy, Vanderbilt University, Nashville, TN 37235, USA
[3] European Space Agency, c/o STScI, 3700 San Martin Drive, Baltimore, MD 21218, USA
[4] Cardiff Hub for Astrophysics Research & Technology, School of Physics & Astronomy, Cardiff University, Queens Buildings, Cardiff, CF24 3AA, UK
[5] Max-Planck-Institut für Astronomie, Königstuhl 17, D-69117 Heidelberg, Germany
[6] Department of Astronomy & Astrophysics and Institute for Gravitation and the Cosmos, The Pennsylvania State University, 525 Davey Lab, University Park, PA 16802, USA
[7] Istituto di Astrofisica e Planetologia Spaziali (INAF-IAPS), Via Fosso del Cavaliere 100, I-00133 Roma, Italy
[8] Centro de Estudios de Física del Cosmos de Aragón (CEFCA), Plaza San Juan 1, E-44001 Teruel, Spain
[9] Department of Astronomy, University of Michigan, 1085 S. University Avenue, Ann Arbor, MI 48109, USA
[10] Department of Astrophysical Sciences, Princeton University, Princeton, NJ 08544, USA
[11] Kavil Institute for Astronomy and Astrophysics, Peking University, Beijing 100871, People's Republic of China
[12] Department of Astronomy, School of Physics, Peking University, Beijing 100871, People's Republic of China
[13] Anton Pannekoek Institute for Astronomy, University of Amsterdam, Science Park 904, 1098 XH Amsterdam, The Netherlands
[14] Department of Physics, University of Nevada, Reno, NV 89557, USA
[15] Nevada Center for Astrophysics, University of Nevada, Las Vegas, NV 89154, USA
[16] Universidad de La Laguna (ULL), Dpto. Astrofísica, Avd. Astrofísico Fco. Sánchez s/n, 38206 La Laguna, Tenerife, Spain
[17] Instituto de Astrofísica de Canarias (IAC), C/Vía Láctea s/n, 38205 La Laguna, Tenerife, Spain
[18] Universitäts-Sternwarte, Fakultät für Physik, Ludwig-Maximilians-Universität München, 81679 München, Germany
[19] George Mason University, Department of Physics and Astronomy, MS3F3, 4400 University Drive, Fairfax, VA 22030, USA
[20] Department of Astrophysics, University of Vienna, Türkenschanzstraße 17, 1180 Vienna, Austria
[21] George P. and Cynthia W. Mitchell Institute for Fundamental Physics and Astronomy, Department of Physics & Astronomy, Texas A&M University, 4242 TAMU, College Station, TX 77843, USA
[22] Shanghai Astronomical Observatory, Chinese Academy of Sciences, Shanghai 200030, People's Republic of China
[23] Department of Physics & Astronomy, University of Southampton, Southampton, Hampshire SO17 1BJ, UK
[24] Department of Physics and Astronomy, University of Kansas, Lawrence, KS 66045, USA
[25] eXtreme Gravity Institute, Department of Physics, Montana State University, Bozeman, MT 59717, USA
[26] Department of Physics and Astronomy, Michigan State University, East Lansing, MI 48824, USA
[27] Department of Physics, 196 Auditorium Road, Unit 3046, University of Connecticut, Storrs, CT 06269, USA
[28] Universite de Strasbourg, CNRS, Observatoire astronomique de Strasbourg, UMR 7550, 67000 Strasbourg, France

Abstract

We present the first results from the Revealing Low-Luminosity Active Galactic Nuclei (ReveaLLAGN) survey, a JWST survey of seven nearby LLAGNs. We focus on two observations with the Mid-Infrared Instrument (MIRI)'s Medium-Resolution Spectrometer of the nuclei of NGC 1052 and Sombrero (NGC 4594/M104). We also compare these data to public JWST data of higher-luminosity AGNs, NGC 7319 and NGC 7469. JWST clearly separates the AGN spectrum from the galaxy light even in Sombrero, the faintest target in our survey; the AGN components have very red spectra. We find that the emission-line widths in both NGC 1052 and Sombrero increase with increasing ionization potential, with FWHM > 1000 km s^{-1} for lines with ionization potential $\gtrsim 50$ eV. These lines are also significantly blueshifted in both LLAGNs. The high-ionization-potential lines in NGC 7319 show neither broad widths nor significant blueshifts. Many of the lower-ionization-potential emission lines in Sombrero show significant blue wings extending > 1000 km s^{-1}. These features and the emission-line maps in both galaxies are consistent with outflows along the jet direction. Sombrero has the lowest-luminosity high-ionization-potential lines ([Ne V] and [O IV]) ever measured in the mid-infrared, but the relative strengths of these lines are consistent with higher-luminosity AGNs. On the other hand, the [Ne V] emission is much weaker relative to the [Ne III] and [Ne II] lines of higher-luminosity AGNs. These initial results show the great promise that JWST holds for identifying and studying the physical nature of LLAGNs.

1. Introduction

As material falls onto a black hole, that material heats up and emits light creating an active galactic nucleus (AGN). While

Table 1
Galaxy Properties

Galaxy Name	Distance (Mpc)	V_{sys} (km s^{-1})	Galaxy Mass $\log(M_\star/M_\odot)$	Morph.	AGN Type	BH Mass $\log(M_\bullet/M_\odot)$	AGN X-ray Lum. $\log(L_X/\text{erg s}^{-1})$	Eddington Ratio $\log(L_{bol}/L_{edd})$
NGC 1052	19.4 ± 0.2	1487.9 ± 5.1	10.71	E4	L1.9	8.82	41.46	−3.97
Sombrero/M104/NGC 4594[a]	9.6 ± 0.3	1090.9 ± 5.1	11.18	Sa	L2	8.83	40.04	−5.66

References. Distances: NGC 1052—Tonry et al. (2001), Sombrero—McQuinn et al. (2016). Systemic velocities V_{sys} are NASA Extragalactic Database heliocentric velocities taken from Fouque et al. (1992) for NGC 1052 and de Vaucouleurs et al. (1991) for Sombrero. Galaxy mass: NGC 1052 and Sombrero from S4G (Sheth et al. 2010; Eskew et al. 2012) with Sombrero corrected to the distance used here. Morphological type: from de Vaucouleurs et al. (1991). AGN type: NGC 1052 and Sombrero from Ho et al. (1997). Black hole (BH) mass: NGC 1052 is based on velocity dispersion (Koss et al. 2022) and Sombrero from Jardel et al. (2011). AGN X-ray luminosity: 2–10 keV luminosities for NGC 1052 from Koss et al. (2022) and for Sombrero from Fernández-Ontiveros et al. (2023) using the updated distance. Eddington ratio: NGC 1052 and Sombrero from Fernández-Ontiveros et al. (2023) using the listed distances and black hole masses.
[a] We adopt "Sombrero" for the galaxy's name in this work.

the most rapidly accreting objects are seen to the edges of our Universe as luminous quasars, the vast majority of central supermassive black holes in nearby galaxies are accreting at less than 1% of their Eddington Limit ($L_{bol}/L_{Edd} < 0.01$; see Ho 2009). These low-luminosity AGNs (LLAGNs) are theorized to have significantly different inner structures from the accretion disks found in more luminous AGNs.

At these low accretion rates, the inner part of the optically thick accretion disk transitions to a hot, optically thin, radiatively inefficient accretion flow (RIAF; Narayan & Yi 1995; Yuan & Narayan 2014; Porth et al. 2019). This change in the central regions of LLAGNs will result in a different ionizing spectrum with fewer far-ultraviolet photons.

Observationally, this is confirmed by the lack of the "big blue bump" in LLAGN spectral energy distributions (SEDs; Ho 1999). This change in ionizing flux is also expected to be reflected in the optical emission-line strengths. Enhanced low ionization emission lines are a key characteristic of low ionization nuclear emission regions (LINERs), which were first identified by Heckman (1980) based solely on optical oxygen lines. LINERs are notably diverse, including sources both with and without clear evidence of an AGN. Multiple radio and X-ray surveys have consistently revealed that most LINERs are powered by LLAGNs (Nagar et al. 2002; Dudik et al. 2005; Nagar et al. 2005; Filho et al. 2006; Flohic et al. 2006; González-Martín et al. 2006; Ho 2008; González-Martín et al. 2009; Hernández-García et al. 2013, 2014). However, LLAGNs are not coincident with LINERs exclusively as many weakly accreting Seyferts are also considered LLAGNs (Kewley et al. 2006; Ho 2009). Optical classification not withstanding, LLAGNs share additional observational signatures. In particular, the dusty torus and broad-line region components may disappear (e.g., Plotkin et al. 2012; Elitzur et al. 2014); and as the Eddington ratio decreases, LLAGNs tend to have stronger jet emission (Ho 2008) and become increasingly radio loud (Ho 2002; Terashima & Wilson 2003; Greene et al. 2006; Panessa et al. 2007; Sikora et al. 2007; Trump et al. 2011). The kinetic energy injected into LLAGN host galaxies by jets may play a significant role in keeping massive early-type galaxies quiescent (Croton et al. 2006; Weinberger et al. 2017). Despite these observational signatures the inner structure of LLAGNs are still not yet well understood and it becomes increasingly difficult to separate out the low-luminosity nuclear emission of a weakly accreting AGN from the surrounding light and obscuring dust of the host galaxy.

Infrared (IR) wavelengths are particularly valuable for studying AGNs (Sajina et al. 2022), as the dust that hides many AGNs at optical and UV wavelengths strongly emits in the IR. In fact, the energy output of many AGNs is highest at X-ray and mid-infrared wavelengths (Prieto et al. 2010). Furthermore, the emission from AGNs at 12 μm has been found to be tightly correlated with their 2–10 keV X-ray emission, with similar luminosities in both bands (Asmus et al. 2015). In addition to the continuum emission from dust or jet emission (e.g., Prieto et al. 2016; Fernández-Ontiveros et al. 2023), strong emission lines are seen at IR wavelengths, including high ionization potential (IP) "coronal" emission lines that track the ionizing spectrum of the AGN (e.g., Satyapal et al. 2008; Goulding & Alexander 2009).

JWST, operating primarily in the IR, is equipped with advanced instruments and brings new opportunities in the study of AGNs. The brightness of AGNs in the IR beyond 2 μm combined with JWST's unprecedented sensitivity at these wavelengths makes it the most sensitive instrument ever for detecting AGNs. For example, the depth reached in just 10 ks of Mid-Infrared Instrument (MIRI) imaging at 12 μm roughly matches that of 2 Ms from Chandra Deep Field North (Xue et al. 2016; assuming the Asmus et al. 2015 relation between the mid-infrared and X-ray emission). The remarkable spatial resolution afforded by JWST's 6.5 m diameter mirror allows us to isolate the LLAGN emission from that of the host galaxy in nearby objects. Finally, JWST's spectral resolution enables studies of line emission profiles that were not possible with previous missions.

The Revealing Low-Luminosity Active Galactic Nuclei (ReveaLLAGN) project, utilizing integral field spectroscopic (IFS) observations from JWST, aims to achieve two primary goals. The first is to provide templates of LLAGN spectra, which can be used to identify the abundant faint AGNs hidden in future JWST data of local and high-redshift galaxies. This includes environments where their presence is currently uncertain, e.g., in dwarf galaxies. Second, through the analysis of the continuum and coronal-line emissions, the project aims to offer valuable constraints for understanding the internal structure of LLAGNs. The study focuses on seven nearby, well-known LLAGNs covering a wide range of both black hole mass ($10^{5.5-9.8}$ $M_\odot$) and Eddington ratio ($\log(L_{bol}/L_{edd})$ ranging from −6.2 to −2.7).

In this paper, we report the first results from the ReveaLLAGN project based on the MIRI Medium-Resolution Spectrometer (MRS) data from our first two targets, Sombrero (also known as M104 and NGC 4594) and NGC 1052. The overall properties of these galaxies are listed in Table 1. These two galaxies have the highest (NGC 1052) and lowest (Sombrero) 12 μm fluxes (Asmus et al. 2014) of all the galaxies in the full ReveaLLAGN sample (A. Seth et al. 2024,

in preparation), and thus represent the full range of signal-to-noise ratios (S/Ns) expected for the survey. NGC 1052 and Sombrero are classified as LINERs based on their optical emission lines (Heckman 1980; Ho et al. 1997)[29] and exhibit extensive multiwavelength emission from their LLAGNs. Hard X-ray observations reveal point sources at the center of both galaxies (NGC 1052: Guainazzi & Antonelli 1999; Kadler et al. 2004b; Sombrero: Fabbiano & Juda 1997; Pellegrini et al. 2002, 2003), accompanied by ultraviolet (UV) variability (Maoz et al. 2005). In the radio domain, NGC 1052 hosts jets at parsec scales with a position angle (PA) $\sim70°$ (Claussen et al. 1998; Kadler et al. 2004b), while at kiloparsec scales the PA of the radio jets is seen at $\sim100°$ (Wrobel 1984; Kadler et al. 2004a). The Sombrero galaxy also contains compact jets, observed at subparsec scales with a PA of $-25°$ (Hada et al. 2013). Additionally, both AGNs' SEDs show a lack of emission in the UV relative to higher-luminosity AGNs (Fernández-Ontiveros et al. 2023), consistent with other LLAGNs (Ho 2008). We review previous observations of both galaxies' AGN in more depth in Section 5.3.

We contrast these two LLAGN observations with previous Spitzer data of higher-luminosity AGNs. We also include JWST MIRI/MRS observations of NGC 7319 (part of the JWST Early Release Observations; Pontoppidan et al. 2022) and NGC 7469 (Armus et al. 2023), two Seyfert galaxies with higher luminosities and Eddington ratios than our targets. The 2–10 keV X-ray luminosities of NGC 7319 and NGC 7469 are $10^{43.1}$ erg s^{-1} and $10^{43.2}$ erg s^{-1} (Ricci et al. 2017), respectively. Their black hole mass estimates are $10^{8.1}\,M_\odot$ and $10^{7}\,M_\odot$ and their Eddington ratios are -1.67 and -0.72 (Koss et al. 2022), respectively. Both galaxies are part of interacting systems and are at larger distances (98.3 and 69.4 Mpc, respectively) than our ReveaLLAGN sample. Despite the increased distances, the higher luminosities result in physically larger line-emitting regions dominated by AGN photoionization, which helps to mitigate the differences in physical length scales between them and our sample. The nuclear spectra of NGC 7319 and NGC 7469 are AGN dominated and point-like at MIRI wavelengths, representing suitable examples of higher-luminosity AGNs with similar spectral resolution and wavelength coverage as our ReveaLLAGN targets.

In Section 4.2 we describe the data acquisition and reduction processes. We present our spectral extraction process and emission-line measurements for both the nuclear spectra and the emission-line maps in Section 3. We present our analysis of the data in Section 4, and discuss them in the context of previous work in Section 5. We conclude in Section 6. We note that all JWST data are barycenter corrected, and thus velocities are given in the barycentric frame.

2. Data Reduction and Methods

2.1. Targets and Data Acquisition

We use JWST MIRI/MRS (Wells et al. 2015) to collect IFS data for our ReveaLLAGN targets in the mid-infrared (4.9–27.9 μm). The full mid-infrared wavelength range for MIRI/MRS is covered by four different channels (channels 1–4): channel 1 (4.9–7.65 μm) and channel 2 (7.51–11.71 μm) use the MIRIFU_SHORT Detector, while channel 3 (11.55–17.98 μm) and channel 4 (17.71–27.9 μm) use the

MIRIFU_LONG Detector. Each channel has an increasing field of view (FOV): channel 1 ($3″2 \times 3″7$), channel 2 ($4″0 \times 4″8$), channel 3 ($5″2 \times 6″2$), and channel 4 ($6″6 \times 7″7$); and pixel size: channel 1 ($0″196$), channel 2 ($0″196$), channel 3 ($0″245$), and channel 4 ($0″273$). All observations were taken using all three MIRI/MRS subchannels.

We describe the observational details for our two ReveaL-LAGN targets; details on the NGC 7319 observation are discussed in Pereira-Santaella et al. (2022). Our Sombrero observations are centered at R.A. = 12:39:59.430, decl. = -11:37:22.99; this position is taken from Gaia EDR3 (Gaia Collaboration et al. 2021). Our NGC 1052 observations are centered at R.A. = 02:41:04.798, decl. = -08:15:20.75 taken from very long baseline interferometry (VLBI) measurements of the AGN (Lambert & Gontier 2009).

Background exposures were taken using offset blank fields selected based on Wide-field Infrared Survey Explorer 12 μm imaging: for Sombrero this field was at R.A. = 12:39:55.9810, decl. = -11:32:11.44 and for NGC 1052 at R.A. = 02:41:5.1200, decl. = -08:12:37.70.

Our MIRI/MRS measurements were taken using the four-point, extended source optimized all-channel dither pattern using the inverted, or negative, dither orientation.[30] This ensures improved sampling of the point-spread function (PSF) at all wavelengths and allows the correction of hot detector pixels. The exposure time for both Sombrero and NGC 1052 was 921.313 s split over four dithers for each subchannel setting. Background exposures used a single dither position with an exposure length of 230.328 s for each subchannel setting. The Sombrero data were among the first science data taken with JWST on 2022 July 4, while the NGC 1052 data were taken on 2022 August 11.

The JWST data presented in this paper were obtained from the Mikulski Archive for Space Telescopes at the Space Telescope Science Institute. The specific observations analyzed can be accessed via DOI:10.17909/n1hq-4p52.

2.2. Data Reduction

We process the raw observations for Sombrero, NGC 1052, and NGC 7319 through version 1.8.2 of the JWST pipeline (Bushouse et al. 2022) using jwst_0989.pmap, which is a versioned reference file that gives overall context for the pipeline. Calibration of our data is divided into three main stages of processing, based on the `Detector1`, `Spec2`, and `Spec3` pipelines.

The `Detector1` pipeline takes the raw counts from the detector, applies basic detector-level corrections to all exposures, and creates uncalibrated countrate images, or lvl2a data products.[31] The `Spec2` pipeline takes the lvl2a products and applies additional instrumental corrections and calibrations to produce a fully calibrated individual exposure, or lvl2b data products. For MIRI/MRS observations, this stage includes adding world coordinate system information, flat-field corrections, and stray light subtraction. We include an optional fringing removal[32] step during this stage to address the significant fringes found in the MIRI/IFU data. The `Spec3` pipeline processes lvl2b spectroscopic observations into lvl3

---

[29] We note that the line ratios of NGC 1052 depends on radius, and are Seyfert-like at smaller radii (Molina et al. 2018)

[30] https://jwst-docs.stsci.edu/jwst-mid-infrared-instrument/miri-operations/miri-dithering/miri-mrs-dithering

[31] See calwebb_detector1 documentation for more information.

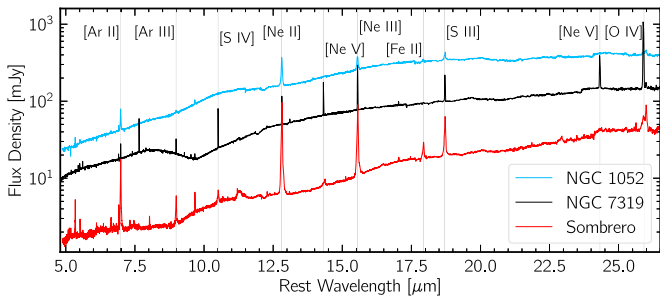[32] See calwebb_spec2 documentation for more information

Figure 1. The first extracted nuclear spectra of ReveaLLAGN targets: Sombrero (red, bottom spectrum) and NGC 1052 (blue, top spectrum). NGC 7319 (black, middle spectrum) is a more distant and more luminous Seyfert 2 AGN and is included to compare our low-luminosity sample to another spectrum taken with JWST MIRI/MRS. Spectra are extracted from an ~1 FWHM radius aperture (see Section 3.1) and are aperture corrected using point-source observations. A subset of strong emission lines are labeled. Also apparent in the spectra at ~10 μm are broad silicate absorption features (in NGC 7319) and emission features (in Sombrero and NGC 1052), and faint polycyclic aromatic hydrocarbon (PAH) emission at 11.3 μm in Sombrero.

data by combining calibrated lvl2b data from associated dithered exposures into a 3D spectral cube or 2D extracted spectra. For MIRI/MRS data the master background subtraction and outlier detection occurs in this stage as well. We choose a final product of four data cubes, one for each channel.[33] The wavelength solution, FLT-4, associated with our pipeline version has a 1σ wavelength calibration error of 10–30 km s^{-1} (Argyriou et al. 2023) throughout the MRS wavelength range.

3. Spectral Extraction and Methods

3.1. Nuclear Spectra Extraction

Nuclear spectra (Figure 1) were extracted using the `photutils` python package's aperture photometry code. At each wavelength, we used a photometric aperture centroided on the median flux image of each channel. The width of this aperture depended on wavelength to account for the changing PSF, with an angular radius of $1.22\lambda/(6.5$ m)–roughly 1 spatial FWHM (FWHM$_{\rm Rayleigh}$); this aperture radius ranges from $0\rlap{.}{''}19$ at 5 μm to $0\rlap{.}{''}97$ at 25 μm. The radius of this aperture at the shorter wavelength $0\rlap{.}{''}19$ corresponds to 8.8, 17.9, and 92 pc in Sombrero, NGC 1052, and NGC 7319, respectively. Background subtraction was done using an annulus with radii between 2 and 2.5× this value.

We created a wavelength-dependent aperture correction based on the MIRI data cube of 10 Lac (obtained from I. Argyriou 2024, private communication). This aperture correction (total/aperture flux) was derived using the same aperture and background annulus as for our galaxy nuclei, with the total flux obtained by integrating the flux of the full data cube. Due to residual sky background issues, we took the median flux of pixels with a radius greater than $6 \times$ FWHM$_{\rm Rayleigh}$ as a background subtraction in each spaxel before calculating the total flux of the data cube at each wavelength. To create a smooth relation, we smoothed the derived aperture correction at each wavelength with a moving median. We compared this smoothed aperture correction to several other point-source observations (HD192163 and HD76534) as well as NGC 1052, which is nearly point-like at longer wavelengths and found generally good agreement (to within ~10%) in the aperture

corrections between sources for channels 1–3, with much poorer agreement and due to noisier measurements in channel 4. The aperture correction declines from values ~2.1 at 5 μm to values similar to the `WebbPSF` prediction (v1.4). We therefore fit a fifth-order polynomial to our smoothed correction in channels 1–3, and set the channel 4 correction to a constant 1.4 value. This aperture correction has been applied throughout this paper.

3.2. Measuring Emission Features

3.2.1. Multi-Gaussian Fitting of the Nuclear Spectrum

Our nuclear spectra have very high S/Ns with clear evidence of many emission lines. These lines often show complex profiles—to extract both flux and velocity information from these lines, we perform multi-Gaussian fits. We first define continuum and fitting windows for each line based on visual inspection—our default fitting window is based on a velocity width of 5000 km s^{-1}. We fit a linear function to the continuum on either side of the emission feature and subtract the result from the data. Next, we utilize the python package `lmfit` to fit both a single-Gaussian and a multi-Gaussian model to the continuum-subtracted emission line. We allow the multi-Gaussian model to consist of up to five components, where each Gaussian component is constrained by the width of the wavelength-dependent MIRI instrument's line-spread function (LSF) and the results of the initial single-Gaussian fits. We select the model with the lowest Bayesian inference criterion as the best-fit model. An example fit to [Fe II] 5.34 μm is shown in the left panel of Figure 2. We do not ascribe any physical interpretation to the individual Gaussian components, instead, we use them to describe accurately the emission-line profile from which we measure the flux, peak velocity, and FWHM$_{\rm model}$. The FWHM$_{\rm line}$ of each emission line is corrected for the width of the MIRI/MRS LSF at the corresponding wavelength, given by

$$\mathrm{FWHM_{line}} = \sqrt{\mathrm{FWHM_{model}^2 - FWHM_{LSF}^2}}. \qquad (1)$$

We use the MIRI MRS LSF width given by Argyriou et al. (2023): FWHM$_{\rm LSF} = c/R$, where c is the speed of light and $R = 4603 - 128 \times \lambda/\mu$m.

Errors on derived quantities are determined from a Monte Carlo (MC) simulation with Gaussian noise added to each pixel based on the standard deviation of the pixels in the continuum windows. The median standard deviation in the continuum pixels is ~4× the formal flux errors provided by the pipeline. Emission-line detections are determined if the integrated flux of the best single-Gaussian emission-line model is above a 5σ threshold. 5σ upper limits are provided for lines without clear detections. We adopt a lower limit on errors for any wavelength-dependent measurement equal to the wavelength calibration error of 30 km s^{-1} provided in Section 2.2. The derived line properties and their associated errors are given in Table 2.

Two key lines of interest for tracing AGN activity are the high-IP lines (IP > 50 eV) [Ne V] 14.32 μm and [O IV] 25.91 μm. However in both our ReveaLLAGN targets, these lines are each blended with a neighboring low-IP line (IP < 20). Specifically, [Ne V] 14.32 μm is blended with the [Cl II] 14.36 μm emission line, while [O IV] 25.91 μm is blended with the [Fe II] 25.98 μm emission line. We deblend the features using a constrained multi-Gaussian model; the low-

---
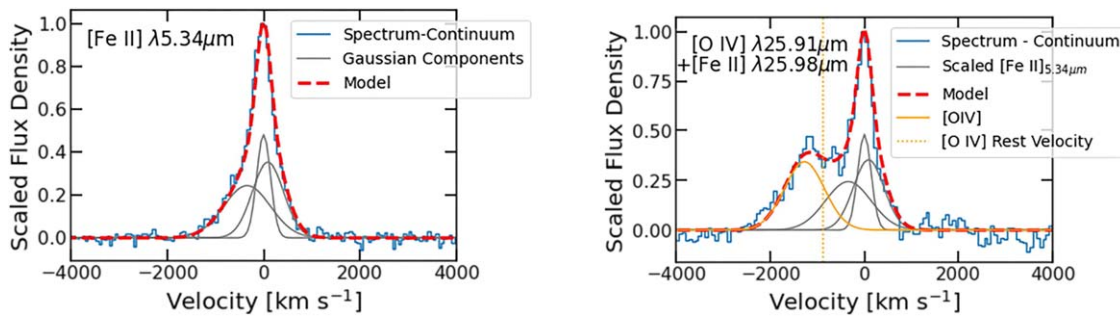
[33] See calwebb_spec3 documentation for more information.

Figure 2. Two examples from Sombrero of the multi-Gaussian models used to characterize emission lines in our sample. Left: the [Fe II] 5.34 μm emission-line fit with a three-component Gaussian model. The gray lines represent individual Gaussian components, while the red dashed line is the sum of those three components. This is the typical method used for characterizing emission features in our data. Right: one of the two coronal lines requiring deblending; here we show the [O IV] 25.91 μm line, which is blended with [Fe II] 25.98 μm; a scaled version of the [Fe II] 5.34 μm line is fit along with a single Gaussian for the [O IV] line. All components are plotted relative to the velocity of [Fe II] 25.98 μm. Markings are as in the left panel, with [O IV] and its expected rest velocity shown in orange.

IP component is fixed to be a scaled version of the [Fe II] 5.34 μm line (Figure 2), an isolated low-IP line with a high S/N. We then allow `lmfit` to fit the [Ne V] 14.32 μm and [O IV] 25.91 μm emission with a single-Gaussian component. To capture the full uncertainty of this measurement we fit the [Fe II] 5.34 μm in each iteration of the MC process before constraining the [Ne V] 14.32 μm and [O IV] 25.91 μm models.

3.2.2. Constructing Emission-line Maps

Outside the nucleus, many lines have low S/Ns, making the multi-Gaussian method we use for the nuclear spectrum less robust. We therefore simplify the Gaussian fitting process used for the nuclear spectra described above by limiting the Gaussian model to a single-Gaussian component. The emission-line flux is calculated by measuring the area under the best-fit Gaussian model, while the velocity is determined by calculating the displacement between the centroid of the best-fit Gaussian model and the rest wavelength of the emission line. For the blended high-IP features (e.g., Figure 2, right), we attempted to deblend them pixel by pixel using two-Gaussian fits, but found no significant detection of the [Ne V] 14.32 μm and [O IV] 25.91 μm emission beyond the central few spaxels due to a combination of low S/N and perhaps the nuclear concentration of these lines. We calculate errors on the flux and velocity using a MC simulation as above, and use a 5σ detection threshold, below which we find our Gaussian fits do not characterize the data well. We discuss the resulting line maps in the Section 4.2.1.

To investigate the ionizing mechanisms of our emission lines, we quantify the spatial extent of the emission region in our line maps by measuring the spatial FWHM (FWHM$_{\rm spat}$) of prominent emission lines. We do this by creating a contour at 50% of the peak flux and calculate 2× the median radius from the peak flux to the contour line. We correct the measured FWHM$_{\rm spat}$ for the MIRI/MRS PSF, which varies by a factor of 5 over the MIRI wavelength range. Using the FWHM of the MIRI/MRS PSF (FWHM$_{\rm MRS}$) taken from Argyriou et al. (2023) we get

$$\mathrm{FWHM}_{\rm spat,corr} = \sqrt{\mathrm{FWHM}_{\rm spat}^2 - \mathrm{FWHM}_{\rm MRS}^2}. \quad (2)$$

The results for this measurement are listed in Table 3 and presented in Section 4.2.2, with discussion given in Section 5.2.

4. Results

4.1. Nuclear Region Emission-line Analysis

4.1.1. Variations with Ionization Potential

In Figure 3 we show the nuclear emission-line properties in our two ReveaLLAGN targets, as well as NGC 7319, ordered by their IP to search for systematic trends. The top panel shows the line luminosity and we find the most luminous detected lines in Sombrero and NGC 1052 are [Ne II] 12.81 μm followed by [Ne III] 15.56 μm which have IPs of 21.56 and 40.96 eV respectively, while in NGC 7319 the [O IV] 25.91 μm line (IP = 54.94 eV) is the most luminous line. More generally, NGC 7319 shows overall higher luminosity in all lines compared to Sombrero and NGC 1052, with the relative luminosity increasing for the higher-IP lines.

The middle panel of Figure 3 shows the FWHM$_{\rm line}$ (see Equation (1)) of each line as a function of IP. These FWHM$_{\rm line}$ values are derived from the best-fit multi-Gaussian model to the nuclear emission lines (Section 3.2.1). The red and blue dashed lines represent arcsecond-level central velocity dispersions for Sombrero and NGC 1052 (Ho et al. 2009), respectively, translated to a FWHM. The emission lines in Sombrero and NGC 1052 are visibly broader than those in NGC 7319 (as can be seen in Figure 1). Specifically, in NGC 7319 the lines have FWHM$_{\rm line} \sim 200$ km s^{-1} regardless of IP. Meanwhile in Sombrero and NGC 1052, all detected lines are significantly wider, with the broadest lines having FWHM$_{\rm line} \gtrsim 1000$ km s^{-1}. A clear trend is also seen with IP in Sombrero with the higher-IP lines having significantly larger FWHM$_{\rm line}$ values. A similar trend is seen in NGC 1052 though with the [Ne VI] 7.65 μm emission feature being notably narrower than the other high-IP lines. A similar correlation is found between FWHM and IP in NGC 7469 (Armus et al. 2023) when comparing the FWHM of the broad components of the emission lines. The widths of these components range from approximately 600 to 1100 km s^{-1}, falling between the ranges seen in NGC 7319 and Sombrero.

Finally, the bottom panel of Figure 3 shows the peak velocity of the emission lines as a function of IP. The peak velocity is measured from our best-fit multi-Gaussian models and we see distinct differences between the galaxies here. For NGC 7319, the peak velocities are quite close to zero at all IPs, which some slightly blueshifted lines ($\sim$50 km s^{-1}) at intermediate IPs. The exception is the [O IV] line, which shows a significant blueshift. We caution that this line is one of the longest wavelength lines we have; the wavelength calibration is

Table 2
Nuclear Spectra Measurements

Galaxy	Line	Wavelength[a] (μm)	IP[b] (eV)	Transition	Flux (10^{-14} erg s^{-1} cm^{-2})	Flux Err. (10^{-14} erg s^{-1} cm^{-2})	Peak Vel. (km s^{-1})	Peak Vel. Err. (km s^{-1})	FWHM$_{line}$ (km s^{-1})	FWHM$_{line}$ Err. (km s^{-1})	S/N	Warning
Sombrero	[Fe II]	5.340	7.90	$^4F_{\frac{9}{2}}$–a $^6D_{\frac{9}{2}}$	0.488	0.004	50	30	530	30	94.5	0
Sombrero	H$_2$	5.448	15.37	(12–10)O(9)	<0.009	…	…	…	…	…	0.0	0
Sombrero	[Mg VII]	5.504	186.76	$^3P_2$–$^3P_1$	<0.020	…	…	…	…	…	1.7	0
Sombrero	H$_2$	5.511	15.37	(0–0)S(7)	0.083	0.003	110	30	300	30	25.8	0
Sombrero	[Mg V]	5.608	109.27	$^3P_1$–$^3P_2$	0.038	0.004	−310	100	1580	110	7.9	0
Sombrero	H$_2$	6.109	15.37	(0–0)S(6)	0.053	0.005	20	30	310	160	12.5	0
Sombrero	[Ni II]	6.636	7.64	$^2D_{\frac{3}{2}}$–$^2D_{\frac{5}{2}}$	0.150	0.004	60	30	900	80	35.2	0
Sombrero	[Fe II]	6.721	7.90	$^4F_{\frac{9}{2}}$–a $^6D_{\frac{7}{2}}$	0.033	0.003	60	30	610	50	9.5	0
Sombrero	H$_2$	6.909	15.37	(0–0)S(5)	0.159	0.003	100	30	390	30	49.9	0
Sombrero	[Ar II]	6.985	15.76	$^2P_{\frac{1}{2}}$–$^2P_{\frac{3}{2}}$	2.320	0.007	30	30	800	30	370.5	0
Sombrero	[Na III]	7.318	47.29	$^2P_{\frac{1}{2}}$–$^2P_{\frac{3}{2}}$	0.064	0.003	−20	30	1020	40	20.8	0
Sombrero	H	7.458	13.60	Pfund–alpha	0.063	0.003	130	30	1130	30	18.5	0
Sombrero	[Ne VI]	7.652	126.25	$^2P_{\frac{3}{2}}$–$^2P_{\frac{1}{2}}$	0.037	0.010	−590	170	2140	550	6.7	0
Sombrero	H$_2$	8.026	15.37	(0–0)S(4)	0.053	0.001	50	30	430	30	32.7	0
Sombrero	[Ar III]	8.991	27.63	$^3P_1$–$^3P_2$	0.403	0.007	20	30	720	50	89.3	0
Sombrero	[Fe VII]	9.527	98.99	$^3F_3$–$^3F_2$	<2.195	…	…	…	…	…	0.1	0
Sombrero	H$_2$	9.665	15.37	(0–0)S(3)	0.140	0.002	90	30	390	30	58.0	0
Sombrero	[S IV]	10.510	34.86	$^2P_{\frac{3}{2}}$–$^2P_{\frac{1}{2}}$	0.222	0.006	0	40	870	100	31.8	0
Sombrero	H$_2$	12.278	15.37	(0–0)S(2)	0.042	0.002	60	30	520	40	16.6	1
Sombrero	H	12.367	13.60	Humph–alpha	0.050	0.004	−130	80	1670	190	15.7	1
Sombrero	[Ne II]	12.814	21.56	$^2P_{\frac{1}{2}}$–$^2P_{\frac{3}{2}}$	6.317	0.020	50	30	590	30	757.2	0
Sombrero	[Ar V]	13.102	59.58	$^3P_1$–$^3P_0$	<0.004	…	…	…	…	…	4.0	0
Sombrero	[Ne V]	14.322	97.19	^3P–$^3P_1$	0.080	0.004	−290	40	1690	140	32.7	0
Sombrero	[Cl II]	14.368	12.97	$^3P_1$–$^3P_2$	…	…	…	…	…	…	13.3	3
Sombrero	[Ne III]	15.555	40.96	$^3P_1$–$^3P_2$	4.101	0.015	40	30	530	30	556.2	0

Notes. The complete table is presented in the online version of the Astrophysical Journal. Here we present the first few rows to show its form and content. The measured quantities provided here are derived from the multi-component Gaussian fits described in Section 3.2.1. We define the line as detected if the integrated flux of a best-fit single-Gaussian model has a S/N $\geqslant$ 5; upper limits are provided for undetected emission lines. The "Warning" column identifies issues with the spectra (blended feature, bad pixel, etc): 0 is a good fit (and measurements reported); 1 is blended/possibly blended features based on visual inspection (measurements are reported); 2 is unacceptable spectra quality with no measurements to report; and 3: no measurements to report due to the deblending procedure (Section 3.2.1, Figure 2).
[a] Rest wavelengths from NIST.
[b] IP energy from NIST.

(This table is available in its entirety in machine-readable form.)

Table 3
Spatial FWHM Measurements of the Resolved Emission Lines

Feature	Rest Wavelength	IP	FWHM$_{MRS}$	Sombrero			NGC 1052		
				FWHM$_{spat}$	FWHM$_{spat,corr}$		FWHM$_{spat}$	FWHM$_{spat,corr}$	
	(μm)	eV	(arcsec)	(arcsec)	(arcsec)	(pc)	(arcsec)	(arcsec)	(pc)
[Fe II]	5.34	7.9	0.27	0.49	0.42	19.45	0.36	0.24	22.34
[Ar II]	6.99	15.76	0.31	0.35	0.17	7.87	0.33	0.12	10.35
[Ar III]	8.99	27.63	0.42	0.46	0.20	9.26	0.41	…[a]	…
[Ne II]	12.81	21.56	0.57	0.62	0.24	11.11	0.58	0.09	8.46
[Ne III]	15.56	40.96	0.63	0.70	0.31	14.35	0.69	0.30	28.22
[S III]	18.71	23.34	0.86	0.99	0.49	22.69	0.86	…[b]	…

Notes. The FWHM of the MRS PSF (FWHM$_{MRS}$) is taken from Argyriou et al. (2023). We combine this with the measured spatial FWHM (FWHM$_{spat}$) via Equation (2) to calculate the corrected FWHM (FWHM$_{spat,corr}$). We only report the lines that we were able to resolve spatially in at least one galaxy. See Section 4.2.2 for details.
[a] FWHM$_{spat}$ measurement unavailable.
[b] Line is unresolved, FWHM$_{spat}$ < FWHM$_{MRS}$.

less accurate at long wavelengths, but is still estimated to be <30 km s^{-1} by Argyriou et al. (2023); this line is also among the most blueshifted lines in Sombrero and NGC 1052.

For Sombrero, the high-IP lines are almost all significantly blueshifted (greater than 3σ from zero), while the lower-IP lines and H$_2$ lines show a slight redshift. The redshift of the H$_2$ lines in Sombrero (median peak velocity of 56 km s^{-1}) may indicate that our systemic velocity taken from H I measurements (de Vaucouleurs et al. 1991) is offset; if this were the case most of the low- and mid-IP lines would show a modest blueshift with a general trend of larger blueshift with higher IP. In NGC 1052, the blueshift in the highest-IP lines are weaker, but there is also a sign of blueshifted emission even at lower IPs. The blueshifted emission could be due to outflows, which we discuss in detail in Section 5.3.

4.1.2. Detailed Nuclear Line Profiles

The high spectral resolution of JWST lets us resolve line widths and look at the detailed shapes of emission lines. Above we found that the high-IP lines show broad, often blueshifted emission lines, and here we look in more detail at the shapes of the lines with the highest S/Ns (>50). Figure 4 shows these lines in each galaxy centered on their expected velocity. Looking at each galaxy, these strong lines show remarkably consistent line profiles suggesting a common physical origin. However, significant differences are seen between galaxies, with Sombrero having a notably asymmetric line profile with blue wings reaching >1000 km s^{-1}, while NGC 1052 and NGC 7319 show more symmetric lines. The strong asymmetry in Sombrero likely indicates the presence of an outflow, which we will discuss in more detail in Section 5.3. Blue asymmetries are also observed in the highest-IP emission-line profiles of NGC 7469 (Armus et al. 2023). The narrower lines in NGC 7319 relative to the other two galaxies are clearly visible as well. We note that the highest-IP lines in NGC 1052 and Sombrero do not have a high enough S/N to examine their line profiles in detail (as well as blending issues in a couple lines) .

4.2. 2D Emission-line Information: Line Maps and Full Width at Half-maximum

4.2.1. Flux and Velocity Maps

Figure 5 shows flux and velocity maps for three lines in both Sombrero and NGC 1052. These are created using the single-

Gaussian fitting method described in Section 3.2.2. Three lines are shown for each galaxy: the H$_2$ 0–0 S(3) line at 9.66 μm, the [Ar II] line at 6.98 μm (IP = 15.76 eV), and the [Ne III] line at 15.56 μm (IP = 40.96 eV). These three lines span a wide range of IPs and critical densities and thus likely trace very different density gas (e.g., Stern et al. 2014). The highest-IP lines (IP > 50 eV) are unresolved, and therefore compact, showing detectable emission only in the central few pixels.

In the Sombrero galaxy, all three lines have similar morphologies, extended east to west with blueshifted emission toward the west. The molecular hydrogen emission has no clear point-like emission and is redshifted relative to the systemic velocity in the nuclear region; this redshift is also seen in several other H$_2$ and low-IP lines in Sombrero (Figure 3). As discussed in the previous subsection, this may be due to the adopted systemic velocity for Sombrero. The velocity dispersion seen in the molecular hydrogen emission maps is quite homogeneous with values up to 240 km s^{-1}, comparable to the measured nuclear stellar velocity dispersion (241 km s^{-1}; Ho et al. 2009). Clear point-like emission is seen in both [Ar II] 6.98 μm and [Ne III] 15.56 μm; this emission appears to be more concentrated in [Ar II] 6.98 μm than [Ne III] 15.56 μm, however this may be due simply to the lower resolution at these wavelengths; we examine this in more detail below in Section 4.2.2. Filaments can be seen extending out to the north and west from the nuclear region in the [Ne III] 15.56 μm flux map. The velocity maps of both ions shown are similar to H$_2$ (redshifted to the east and blueshifted to the west), but show complex velocity fields, e.g., a patch of blueshifted emission ~2″ east of the nucleus and a stretch of redshifted emission stretching southeast from the nuclear region. The velocity dispersion in [Ar II] 6.98 μm and [Ne III] 15.56 μm both peak in the nuclear region with a maximum velocity of about 500 km s^{-1}.

In NGC 1052, the H$_2$ emission-line map differs significantly from the [Ar II] 6.98 μm and [Ne III] 15.56 μm emission. The H$_2$ emission-line flux maps have a weak peak in the nuclear region and extend northeast to southwest. The velocity maps of H$_2$ are blueshifted in the northeast and redshifted to the south and west. The velocity dispersion is larger along the minor axis of rotation and peaks at ~275 km s^{-1} in the nuclear region, a bit higher than the Ho et al. (2009) central stellar velocity dispersion of 215 km s^{-1}. The H$_2$ flux, velocity, and dispersion maps presented here for NGC 1052 are in agreement with Müller-Sánchez et al. (2013) where the H$_2$ 1–0 S(1) line
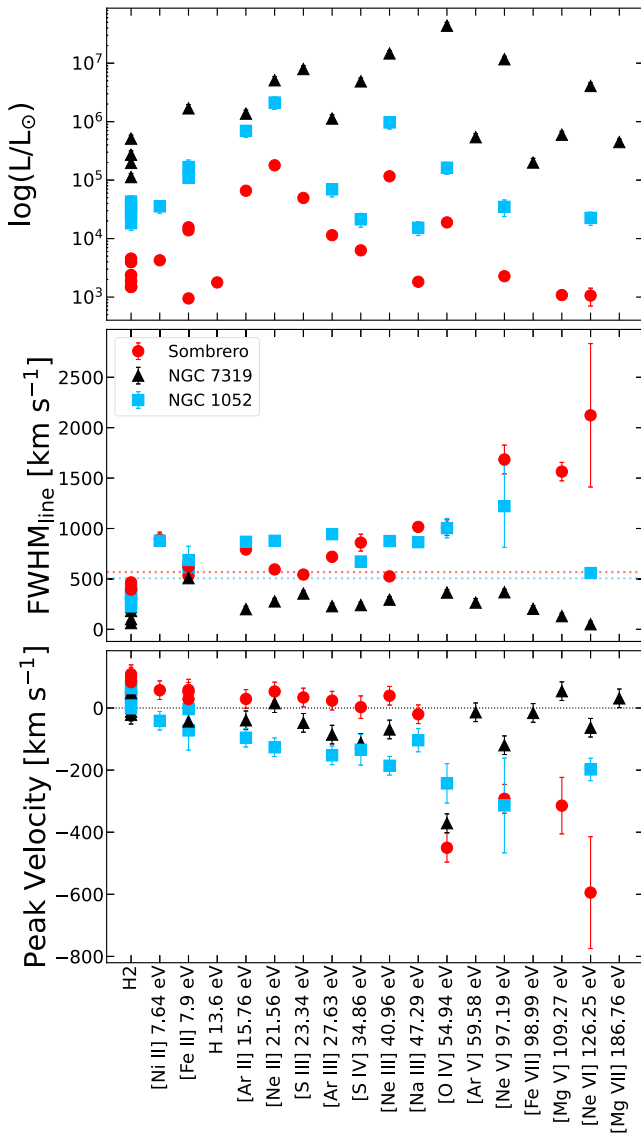
Figure 3. Emission-line trends with IP. Emission features are listed along the *x*-axis ordered by their IP. Top: luminosity vs. IP. The emission-line luminosities scale with the Eddington ratio of the source. NGC 7319 has the highest Eddington ratio and the most luminous emission lines, followed by NGC 1052, and then Sombrero. The luminosities have a median fractional error of 15%. Middle: FWHM$_{line}$ vs. IP. The FWHM$_{line}$ values of the emission features increase with IP in Sombrero and NGC 1052 while the FWHM$_{line}$ values of the NGC 7319 emission features stay relatively constant with IP. The FWHM$_{line}$ values in units of km s^{-1} are shown on the *y*-axis with a median error of 30 km s^{-1}. Red and blue dashed lines represent the central stellar velocity dispersion measurements from Ho et al. (2009) translated to a FWHM. Bottom: peak velocity vs. IP. The peak velocities of the emission lines show a trend of becoming increasingly blueshifted with increasing IP in Sombrero and NGC 1052. The *y*-axis shows the peak velocity of the best-fit Gaussian model with a median error of 30 km s^{-1}.

at 2.12 μm was examined using SINFONI, benefiting from slightly better spatial resolution. Müller-Sánchez et al. (2013) interpret the morphology and kinematics of H$_2$ as a decoupled rotating disk, due to the gas having a kinematic major axis that is not aligned with the stellar rotation axis. Our H$_2$ flux map is also similar in morphology to the CO gas seen with Atacama Large Millimeter/submillimeter Array in Kameno et al. (2020), which they interpret as a circumnuclear disk. The [Ar II] 6.98 μm and [Ne III] 15.56 μm emission-line flux maps are
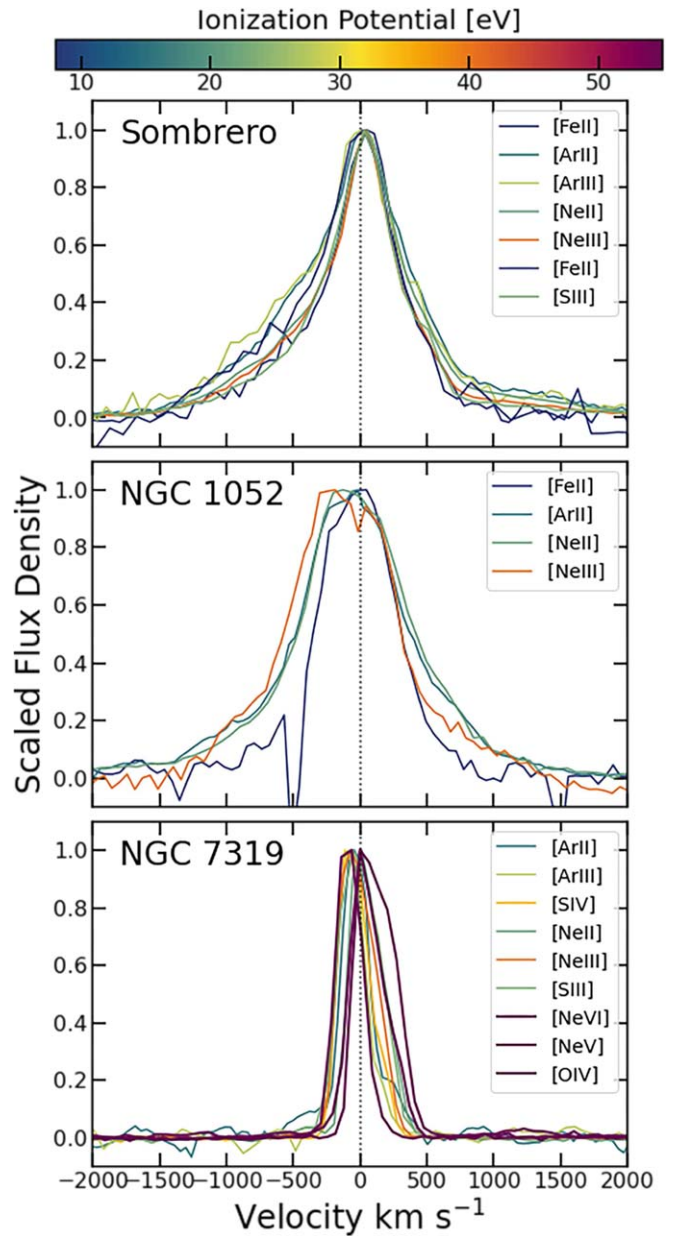
Figure 4. Nuclear emission-line profiles with S/N > 50 centered on the expected velocity. Sombrero lines are asymmetrical with a blueshifted extension, or wing, while NGC 1052 and NGC 7319 have generally more symmetric profiles with blueshifted peaks. Emission lines in NGC 7319 show redshifted extensions at high IPs.

strongly peaked in the nucleus and share a roughly concentric radial profile. The corresponding velocity maps of NGC 1052 reveal extended emission with a distinct kinematic structure characterized by a heavily blueshifted region directly east of the nucleus and a heavily redshifted region to the west, with velocities up to 590 km s^{-1}. As detailed in Section 1, NGC 1052 has an inner radio jet on ~2 pc scales with a PA ~ 70° (Claussen et al. 1998; Kadler et al. 2004b), while at larger scales (~1 kpc) the PA of the radio jets is approximately 100° (Wrobel 1984; Kadler et al. 2004a). Our MIRI/MRS data fall between these two scales, and the PA of the kinematic structure we see (Figure 5) falls between the PAs of these inner and outer jets.
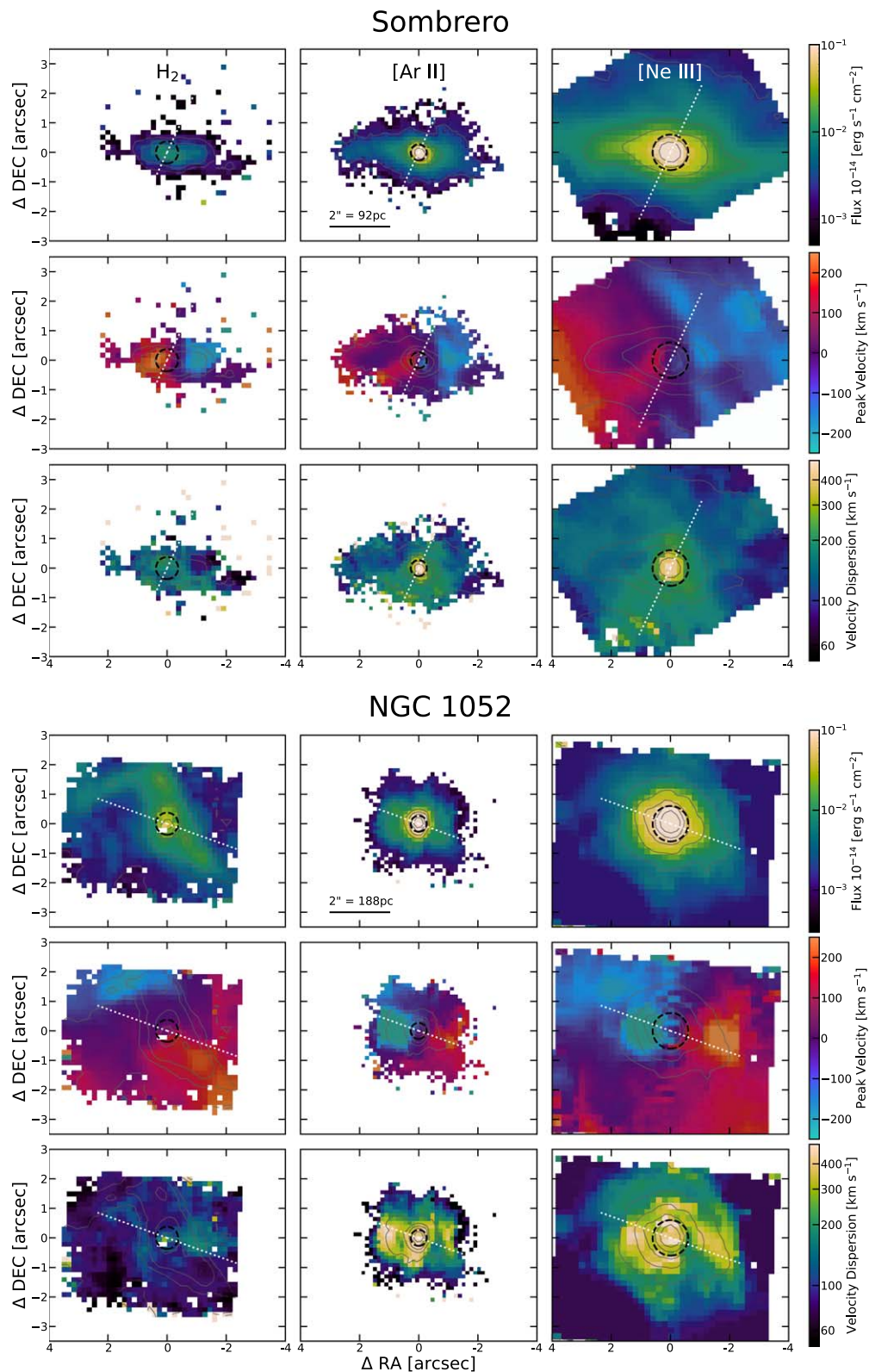
Sombrero

NGC 1052

Figure 5. Flux, velocity, and dispersion maps for three emission lines in both Sombrero and NGC 1052. In all maps north is up and east is to the left. The leftmost column shows the H_2(0–0)S(3) molecular hydrogen line at 9.66 μm, the middle column shows the low-IP line [Ar II] 6.98 μm, and the right column shows the mid-IP line [Ne III] 15.56 μm. Contours indicate flux levels of 1%, 5%, 10%, 25%, and 50% of the peak line flux, while the dashed black line represents the aperture used to extract the nuclear spectrum at that wavelength. The white dotted lines (shown with arbitrary length) indicate the orientation of compact radio jets; corresponding to a PA of $-25°$ in Sombrero oriented nearly along our line of sight (Hada et al. 2013), and a PA of $70°$ in NGC 1052 oriented along the plane of the sky (Kadler et al. 2004b).
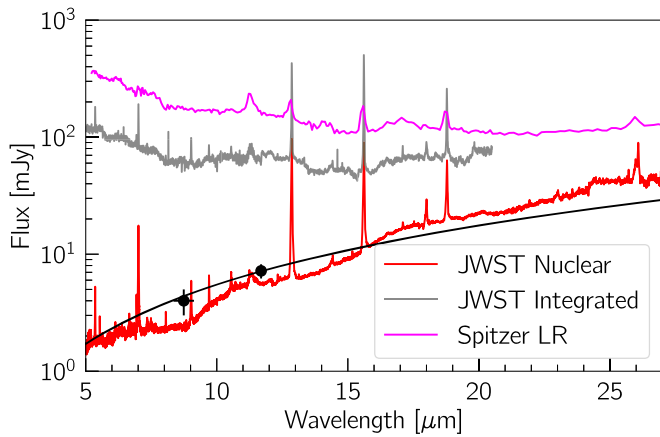
Figure 6. JWST enables us to separate LLAGN spectra from their host galaxy. Comparison of the aperture-corrected nuclear extracted spectrum in Sombrero (red line; same as Figure 1), to the integrated MIRI/MRS spectrum (gray line; FOV = $6\rlap{.}''6 \times 7\rlap{.}''7$), and the Spitzer LR spectrum (magenta line; FOV = $27\rlap{.}''7 \times 51\rlap{.}''8$). The black line shows the best-fit high-spatial-resolution power-law fit to Sombrero from Fernández-Ontiveros et al. (2023): this line is fit to the black points, which are photometry from Gemini (Asmus et al. 2014), the Very Large Telescope (Fernández-Ontiveros et al. 2023), as well as subarcsecond data at shorter wavelengths; both the data and fit are in good agreement with our nuclear spectrum. We show the integrated spectrum only out to 20 μm as the poorly constrained MIRI channel 4 background levels significantly impact the integrated spectrum measurements at redder wavelengths.

4.2.2. Spatial Full Width at Half-maximum Measurements

Following the methodology outlined in Section 4.2.1, we determine $\mathrm{FWHM_{spat,corr}}$, characterizing the PSF-corrected spatial extent, for six emission lines in Sombrero and four emission lines in NGC 1052. These lines are at low- and mid-IP and have sufficient S/Ns to enable the measurement. The $\mathrm{FWHM_{MRS}}$, $\mathrm{FWHM_{spat}}$, and $\mathrm{FWHM_{spat,corr}}$ measurements are provided in Table 3. Overall, we find that the lines in NGC 1052 are either unresolved or just barely spatially resolved, with the [Ne III] line having the largest spatial extent ($\mathrm{FWHM_{spat,corr}} = 0\rlap{.}''30$, or 28.2 pc). On the other hand, all the emission lines in Sombrero are spatially resolved, with $\mathrm{FWHM_{spat,corr}} > 0\rlap{.}''17$, or 8 pc, and no clear trend with IP. We note that while $\mathrm{FWHM_{spat,corr}}$ estimates were not possible for the high-IP coronal lines ([O IV] 25.91 μm and [Ne V] 14.32 μm), these lines do appear to be quite compact in both galaxies. In both galaxies, the [Ne III] 15.56 μm emission is more extended than the [Ne II] 12.81 μm emission, a somewhat surprising result that we discuss further in Section 5.2.

5. Discussion

In this section we present our results in the context of previous work. First, in Section 5.1, we discuss the power of JWST in separating LLAGNs from their host galaxies. Then in Section 5.2, we compare the nuclear emission features from our LLAGNs to AGNs of varying types, and end with Section 5.3 by discussing evidence for outflows seen in the LLAGN spectra.

5.1. The Promise of JWST for Revealing Low-luminosity Active Galactic Nuclei

In Figure 6 we show a comparison of the extracted nuclear spectrum (see Section 3.1) in Sombrero to both the integrated

flux in the JWST data cube, and the Spitzer LR spectrum from the SINGS survey (Kennicutt et al. 2003). The integrated flux was calculated by summing all spaxels in each MIRI data cube. Since the FOV varies between each channel, we normalized the integrated spectrum to channel 4. In this channel the FOV measures $6\rlap{.}''6 \times 7\rlap{.}''7$ corresponding to a physical scale of 306×357 pc^2 at the distance of Sombrero. Note that the integrated spectrum is not shown at the longest wavelengths due to sky subtraction issues as discussed in Gasman et al. (2023).

The nuclear emission clearly shows an SED that increases with wavelength, while the integrated data cube has a very different SED. Just $\sim$1% of the flux in the JWST integrated cube is coming from the nuclear component at 5 μm, while the nuclear compoment is >10% of the flux by 20 μm. This rising nuclear SED is consistent with two previous photometric measurements of Sombrero at high resolution (black points/line in Figure 6) and within the expectations of LLAGN spectra (Fernández-Ontiveros et al. 2023). However, the information available in the nuclear spectrum is clearly far richer than was available with previous ground-based photometric measurements.

The two larger-scale spectra from both Spitzer and our integrated JWST data in Figure 6 show very different spectral shapes that are dominated by galaxy emission. The shapes of these two spectra are in good agreement despite the different apertures, suggesting a roughly constant SED for the galaxy component. Overall, the data show that even in Sombrero, the faintest target in the ReveaLLAGN survey, we can cleanly extract the LLAGN emission and separate it from its surrounding galaxy. Although the primary goal of this paper is analysis of the emission lines in our ReveaLLAGN MIRI spectra, the continuum shape also encodes information on the emission mechanisms of these LLAGNs. High-angular-resolution work on LLAGNs has consistently shown jet-dominated emission to follow a broken power-law continuum (Ho et al. 1996; Chary et al. 2000; Prieto et al. 2016; Fernández-Ontiveros et al. 2023) which is consistent with self-absorbed synchrotron emission characteristic of compact jet emission (Marscher & Gear 1985).

While Figure 6 shows broad agreement with a single power-law fit from Fernández-Ontiveros et al. (2023) over the MIRI wavelength range, there is also considerable complexity seen in the SEDs (Figure 1), with a clear inflection point in the Sombrero nuclear spectrum at 9 μm. We also see a gradual flattening of the spectrum at long wavelengths in NGC 1052, which is consistent with the turnover of the broken power law below 20 μm and the nuclear fluxes at lower frequencies (Fernández-Ontiveros et al. 2019). The complexity of the continuum shapes we see in the MIRI spectra suggest additional information may be available from detailed fitting of the continuum that includes the contributions of broad silicate features (J. A. Fernández-Ontiveros et al. 2024, in preparation).

5.2. The Emission Lines of Low-luminosity Active Galactic Nuclei: Comparison to Previous Work

In this subsection, we focus on comparing the nuclear emission-line luminosities and ratios to previous measurements of typically much higher-luminosity AGNs.

Figure 7 compares the luminosities of the two high-IP lines detected in all three galaxies, [Ne V] 14.32 μm and [O IV] 25.91

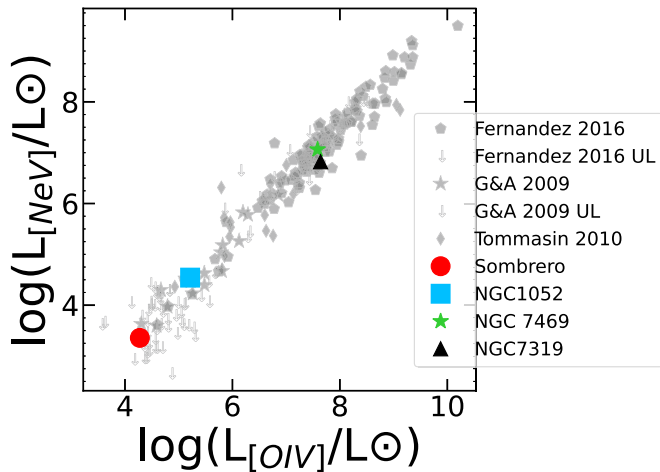**Figure 7.** Sombrero and NGC 1052 have very low-luminosity detections of [Ne V] 14.32 μm and [O IV] 25.91 μm, with [Ne V] 14.32 μm in Sombrero having one of the lowest-luminosity detections to date. A tight, nearly linear relationship can be seen when comparing the luminosities of coronal lines [O IV] 25.91 μm (x-axis) and [Ne V] 14.32 μm (y-axis). The logarithm of the luminosity on both axes is shown in solar units (3.846×10^{33} erg s^{-1}). Gray markers represent results from previous surveys (Goulding & Alexander 2009; Tommasin et al. 2010; Fernández-Ontiveros et al. 2016) with upper limits on [Ne V] found in Goulding & Alexander (2009) and Fernández-Ontiveros et al. (2016). The green star represents measurements for NGC 7469 taken from Armus et al. (2023)

μm, to literature measurements primarily from Spitzer (Goulding & Alexander 2009; Tommasin et al. 2010; Fernández-Ontiveros et al. 2016). We note that these data have much lower physical resolution than our nuclear JWST data, and thus contamination of the AGN spectra by galaxy light is likely significant in some cases, especially for lower-IP lines discussed below that are excited by sources other than the AGN. NGC 7319 and NGC 7469, as expected, have luminosities very typical of previously measured AGNs, while Sombrero has the lowest luminosities of both lines compared to any previous measurements. While Sombrero and NGC 1052 stand out as being very low-luminosity detections, they both follow the tight, nearly linear correlation between these two coronal lines that is seen across a wide range of AGNs (Goulding & Alexander 2009).

Comparing the ionized states of a particular atom enables us to study the ionization structure within an AGN more clearly. In this regard, the mid-infrared is particularly valuable as it contains multiple neon emission lines at different ionizations. In Figure 8 we compare the flux values of [Ne II] 12.81 μm, [Ne III] 15.56 μm, and [Ne V] 14.32 μm from our sample to previous surveys. Comparing line fluxes (rather than luminosities) ensures that the correlations seen are the result of excitation differences, and not caused by observing sources at a range of distances (which can create false correlations between line luminosities).

The left panel comparing [Ne V][34] and [Ne III] shows a roughly linear correlation that gets tighter with increasing [Ne V] flux. Sombrero has significantly weaker [Ne V] than other sources with similar [Ne III] flux, and many of the lower-luminosity sources including NGC 1052 also scatter toward fainter [Ne V] flux relative to the relation seen at higher line fluxes. Thus Sombrero is an outlier, but follows the qualitative

trend of lower [Ne V] luminosities that are seen in other lower-luminosity AGNs. The middle panel comparing the flux of [Ne II] to [Ne V] shows similar results to the left panel, but with a much looser relation seen between the lines at high line fluxes. Finally the right panel shows that the relative [Ne II] and [Ne III] fluxes fall within the range of previous measurements in all three galaxies. This suggests that these lower-IP lines have values typical of higher-luminosity AGNs, and it is the [Ne V] line that is weaker than in other sources.

We combine the information on all three neon lines in Figure 9, which compares the ratios of [Ne V]/[Ne II] and [Ne III]/[Ne II]. The ratio of [Ne V] to [Ne II] has been employed as a diagnostic tool in IR spectra to assess the contribution of AGN activity (Goulding & Alexander 2009; Sajina et al. 2022). Since [Ne V] can only be formed through AGN processes, and [Ne II] can arise from both AGN and non-AGN mechanisms, this ratio helps determine the presence and influence of AGNs. We emphasize again that the literature data here have low spatial resolution, and therefore any line emission in the central kiloparsecs of the galaxies contain significant contamination from the host galaxy. NGC 1052 and especially Sombrero fall well below the main trend line found in Figure 9 and into a region only populated with upper limits of [Ne V] from the other surveys.

We can get a sense of the level of galaxy contamination in our own JWST spectra by comparing the extent of emission features with different IPs, and in Section 4.2.2 we find that the $FWHM_{spat,corr}$ values of the [Ne II] and [Ne III] emission lines are quite compact. We would expect [Ne II] be more spatially extended than higher-IP lines, including [Ne III], since [Ne II] lines come predominantly from star formation. This is not what we find in either source; in fact [Ne II] is found to be more compact than [Ne III] in both NGC 1052 and Sombrero. The fact that [Ne II] emission is compact does not strictly mean that it comes from the AGN; it could simply mean that any star formation is also compact/unresolved. While Prieto et al. (2014) report the presence of extended Hα emission perpendicular to the jet in Sombrero, which may be associated with star formation, they find no conclusive evidence of star formation, from UV to IR, within parsecs of the center of Sombrero, nor in NGC 1052 (Prieto et al. 2021). A lack of excitation from star formation is consistent with the absence of any PAH emission in the nuclear spectra of NGC 1052 and only a weak PAH signature at 11.3 μm in Sombrero (Figure 1). This lack of evidence for star formation suggests that the nuclear line ratios of our targets (Figure 9) are not significantly contaminated by emission from star formation, and that the outlier status of our two galaxies is the result of very low-luminosity detections of [Ne V] made possible by the spatial and spectral resolution of JWST. The differences we see then in Figure 8 are due to excitation differences from the AGN accretion structure. This difference can be explained by either a change in SED or very low ionization parameters that result in a deficiency of the high-energy photons ($\gtrsim$100 eV) needed to excite the line. This conclusion is consistent with previous work on LLAGNs (Ho 2008; Eracleous et al. 2010), including photoionisation models for compact jet synchrotron emission (Fernández-Ontiveros et al. 2023), shock excitation models (Dopita et al. 2015), and the expectations of a central engine with advection-dominated accretion flows (Nemmen et al. 2014). We will be able to test this result and compare this to models of AGN ionization once the full RevealLLAGN sample is available (J. A. Fernández-Ontiveros et al. 2024, in preparation).

---

[34] For the rest of the discussion, we will refer to [Ne II] 12.81 μm, [Ne III] 15.56 μm, and [Ne V] 14.32 μm as [Ne II], [Ne III], and [Ne V], respectively.
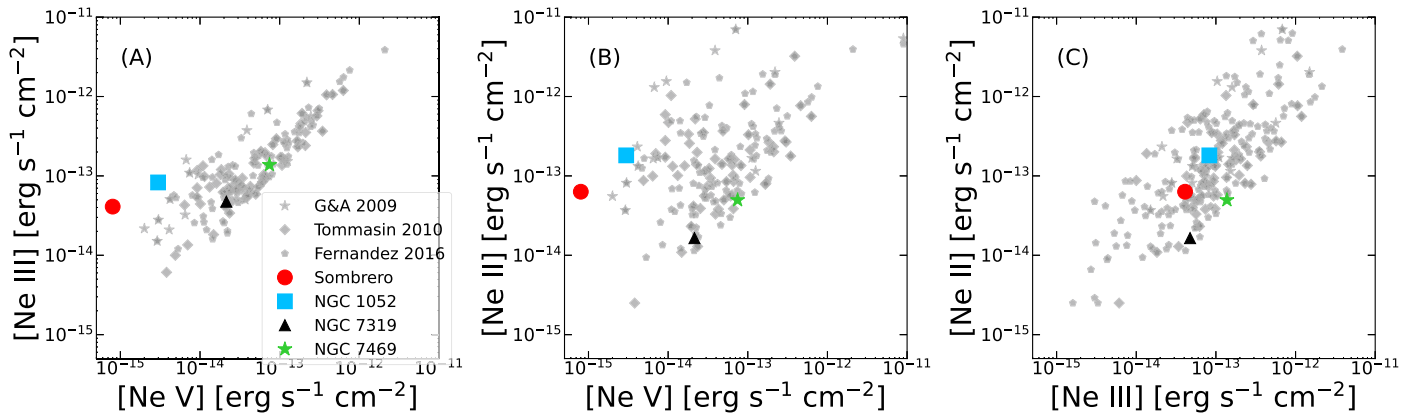
Figure 8. Flux measurements of different ionized states of neon from our sample compared to previous AGN surveys. The [Ne V] 14.32 μm flux from our sample, especially in Sombero, is much lower than in previously observed AGNs relative to the [Ne III] 15.56 μm (plot A) and [Ne II] 12.81 μm (plot B) fluxes. However, the [Ne II] and [Ne III] fluxes are fairly typical of other AGNs (plot C). Units on all axes are in erg s^{-1} cm^{-2}. Markers are the same as in Figure 7.
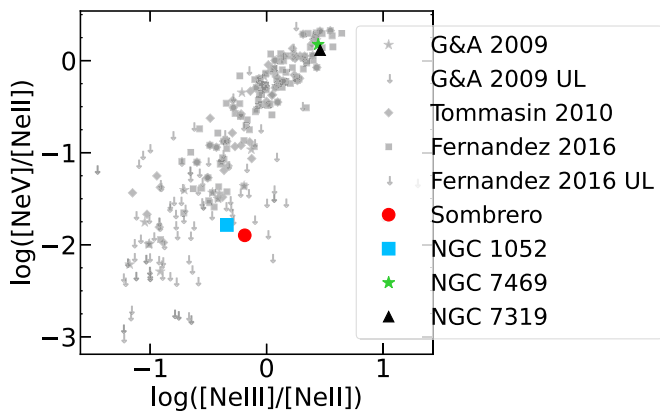

Figure 9. The low-luminosity detections of [Ne V] place our LLAGN sample well below the trend line when comparing the logarithm of [Ne III] 15.56 μm/ [Ne II] 12.81 μm (x-axis) to the logarithm of [Ne V] 14.32 μm/[Ne II] 12.81 μm (y-axis). Marker colors are the same as in Figures 7 and 8.

5.3. Outflows in NGC 1052 and Sombrero

In Section 4.1, we identify the following emission-line features in NGC 1052 and Sombrero:

1. an increase in line width with IP,
2. an increase in blueshifted emission with IP,
3. broad emission in the weakly detected high-IP and coronal lines, and
4. prominent blue wings in the high-S/N lines of Sombrero.

The trend of increasing line width and IP was originally attributed to cloud stratification—the coronal lines are emitted from denser clouds closer to the central engine, which are subject to more intense ionizing flux (Filippenko & Halpern 1984; Filippenko 1985; Appenzeller & Oestreicher 1988; Filippenko & Sargent 1988). Recent work has confirmed that many Seyfert galaxies, regardless of brightness or AGN type, show an increase in both line FWHM and line blueshifting with increasing IP (e.g., Rodríguez-Ardila et al. 2006, 2011; Armus et al. 2023). Furthermore, there are known correlations between blueshifted emission and both increasing IP in coronal lines and increasing line width in the [O III] line in narrow-line Seyfert 1 galaxies (e.g., Komossa et al. 2008). While there is clear evidence that coronal-line emission and their profiles are driven mainly by photoionization from the AGN (e.g., Nussbaumer & Osterbrock 1970; Korista & Ferland 1989;

Oliva et al. 1994; Pier & Voit 1995; Rodríguez-Ardila et al. 2011), other work has demonstrated that outflows are needed to explain fully the observed emission (e.g., Appenzeller & Oestreicher 1988; Erkens et al. 1997; Wilson & Raymond 1999; Rodríguez-Ardila et al. 2006; Müller-Sánchez et al. 2011; Rodríguez-Ardila et al. 2011). In fact, the blueshifted emission even at mid IPs could trace outflowing material closer to the AGN than the narrower emission, with the line asymmetry being caused by redshifted emission being absorbed along the line of sight (Komossa et al. 2008).

Given the known importance of outflows and shocked emission in LINERs (e.g., Ho 2008; Trump et al. 2011; Molina et al. 2018), we conclude that the emission-line features identified above are indicators of outflows for both Sombrero and NGC 1052. We discuss other evidence and the possible origins of the outflows in NGC 1052 and Sombrero below.

5.3.1. Previous Evidence of Outflows in NGC 1052

Previous work has demonstrated the presence of AGN-related outflows in NGC 1052 on multiple spatial scales. Optical IFS studies of NGC 1052 show evidence for an outflow from the AGN on larger scales (Sugai et al. 2005; Dopita et al. 2015; Dahmer-Hahn et al. 2019; Cazzoli et al. 2022). The outflow is roughly aligned with the radio jet (Claussen et al. 1998; Kadler et al. 2004b), with a PA $\sim 70°$ and is generally in good agreement with the velocity structures seen in Figure 5. These studies also find a broad Hα and Hβ component with a width ~ 3000 km s^{-1}; this is significantly broader than the widths of the mid and high-IP lines we see here.

Similarly, on much smaller spatial scales, Müller-Sánchez et al. (2013) find evidence of outflows in the velocity dispersion maps of H$_2$ emission seen in the IR, while Pogge et al. (2000), Walsh et al. (2008), and Molina et al. (2018) found evidence for outflows in Hubble Space Telescope (HST) data. Both Pogge et al. (2000) and Walsh et al. (2008) found evidence for strong outflows as well as ionized regions associated with jet-like features. Meanwhile, Molina et al. (2018) demonstrated that shocked emission likely originating from these outflows is the dominant power source at just ~ 20 pc outside of the galaxy center. Similar to Dopita et al. (2015), Cazzoli et al. (2022), and this work, Molina et al. (2018) found that the shock-dominated, off-nuclear emission lines had widths consistent with $v \lesssim 500$ km s^{-1}. They also found broad Hα and Hβ emission in the unresolved AGN spectrum, with

FWHM $\sim 10^3$ km s^{-1}. We note that a majority of the emission seen in Molina et al. (2018) lies within the JWST nuclear aperture used in this work.

5.3.2. Previous Evidence of Outflows in Sombrero

Given the low accretion rate and the presence of a small-scale radio jet, Sombrero likely has strong radio outflows (Meier 2001; Fender & Belloni 2004). In fact, Walsh et al. (2008) determined that while Sombrero has organized motion within the central 0″5 consistent with an overall rotation pattern, there are significant irregularities that could be caused by outflows. Pogge et al. (2000) also found evidence of turbulent motion via spiral-like wisps in narrowband Hα + [N II] imaging. Emsellem & Ferruit (2000) further identified a strong velocity gradient near the galaxy center, and noted that the kinematics of the gas within the central 1″ was decoupled from the gas in the spiral wisps. These east–west oriented wisps are not well aligned with the inner radio jet described by Hada et al. (2013) and Mezcua & Prieto (2014), which runs along the north–south axis and is oriented toward our line of sight. We note that the presence of broad Hα is unclear, with two analyses of the same HST spectra coming to different conclusions (Walsh et al. 2008; Hermosa Muñoz et al. 2020). Mason et al. (2015) found that the near-infrared SED appears to be similar to that of other type 2 LINERs, and Gallimore et al. (2006) and Li et al. (2011) also found evidence for larger-scale outflows in Sombrero using radio and X-ray data, respectively.

5.3.3. Origins of the Outflows

Here we consider two possible models for the outflows seen in NGC 1052 and Sombrero. We note that radiation-pressure-driven outflows do not significantly contribute to the outflows seen in LLAGNs (Meena et al. 2023), and therefore we do not discuss them below. As a reminder, both of these objects are classified as LINERs and exhibit low Eddington ratios (Table 1), with evidence of compact radio jets (Sections 1; 4.2.1).

Winds launched from the RIAFs. Unlike traditional cold, thin-disk models, RIAFs occur when the accretion rate is sufficiently low that the inner disk puffs up and becomes a hot, advection-dominated accretion flow (Narayan & Yi 1995; Blandford & Begelman 1999; Yuan & Narayan 2014). Previous empirical studies showed that radio outflows from AGNs, including those with thin-disk accretion flows and RIAFs, increase in strength as the accretion rate decreases (e.g., Ho 2002; Meléndez et al. 2010). RIAFs extending to large scales can eliminate broad-line emission (Elitzur & Ho 2009) and the "big blue bump" associated with thin-disk accretion (e.g., Trump et al. 2011); the corresponding lack of UV emission and broad-line features in most LINER AGNs (e.g., Nicastro et al. 2003; Ho 2008) suggest they may be powered by RIAFs.

The strong wind along the polar or jet direction in RIAFs that was predicted by magnetohydrodynamical numeral simulations (Yuan et al. 2012, 2015) has been observationally confirmed in recent years (e.g., Wang et al. 2013; Cheung et al. 2016; Park et al. 2019; Shi et al. 2021). These energetic winds originate in the coronal region of the accretion flow, implying that higher-IP lines would experience more intense outflows, and thus likely have larger widths, consistent with the findings

presented in Section 4.1. Given their low accretion rates (see Table 1), the absence of the "big blue bump" in both of their SEDs (Fernández-Ontiveros et al. 2012), and the lack of clear broad Hα emission in Sombrero (Walsh et al. 2008), it is likely that both NGC 1052 and Sombrero are powered by an RIAF. Therefore, we conclude that the energetic winds driven by the hot accretion flows in both LLAGNs likely contribute to the observed emission. However, we note that by their nature RIAFs do drive radio jets, and as such these winds may not be the sole explanation for the observed outflows.

Jet-driven outflows. Jets associated with AGN accretion are known to drive outflows that create shocked emission and can regulate the star formation rate in the galaxy (e.g., Silk & Rees 1998; Weinberger et al. 2017; Davé et al. 2019). In fact, while we did not find any trends with IP in the nuclear spectra of NGC 7319, Pereira-Santaella et al. (2022) found that high-IP coronal-line emission is detected close to the hot spots of the known radio jet, which they conclude indicates the presence of a jet-driven outflow.

Due to their less luminous, lower-accretion rate engines, the shocked emission driven by jets or outflows can often dominate over photoionization at small distances from the nuclei in LLAGNs (Molina et al. 2018). Furthermore subparsec-scale radio jets occur more frequently in LINERs (Nagar et al. 2005), which could further indicate the presence of jet-driven outflows.

Recent work by Meenakshi et al. (2022) demonstrated that small-scale jets can produce large widths even in mid-IP lines like [O III] λ5007, similar to the widths seen in our mid-IP lines studied here. They also conclude that similar widths can be seen in the different gas phases of the ISM, which appears to be somewhat qualitatively true for NGC 1052—the observed positive correlation between IP and FWHM in NGC 1052 in Figure 3 is much less pronounced than that in Sombrero. Furthermore, both Sugai et al. (2005) and Dopita et al. (2015) found evidence that the jet in NGC 1052 was interacting with the circumnuclear gas.

In both the RIAF- and jet-driven wind scenarios, the orientation of the jet should impact the observable signatures. In Sombrero, modeling of VLBI data suggests the inner jet is oriented close to our line of sight (Hada et al. 2013), while in NGC 1052, the jet is oriented more in the plane of the sky (Kadler et al. 2004b). This difference in jet orientation may be the reason why only Sombrero shows blueshifted emission in its nuclear spectrum, while the ionized emission-line maps in NGC 1052 show strong strong blue- and redshifts oriented close to the jet axis (Figure 5). However, since both RIAF- and jet-driven winds will result in an outflow in the jet direction, a combination of SED modeling on the smallest scales with emission-line analysis like that presented here is likely required to resolve what drives the outflows in LLAGNs.

6. Conclusions

This paper features the first observations of the ReveaL-LAGN survey, a JWST project to characterize seven nearby LLAGNs. We present MIRI/MRS data of the least and most luminous targets in our sample, Sombrero and NGC 1052, respectively. We compare these data to those of higher-luminosity AGNs, specifically NGC 7319 and NGC 4395. We characterize the numerous emission lines seen in the nuclear spectrum and create line maps across the MRS FOV for stronger lines.

We find the following results.

1. The resolution and sensitivity of JWST allows us to separate the AGN continuum and emission lines cleanly from the surrounding galaxy even in our least luminous target, Sombrero.

2. The ionized emission lines in both Sombrero and NGC 1052 are broad, and have widths that increase with increasing IP, reaching FWHM > 1000 km s^{-1}. The highest-IP lines (IP > 50) show blueshifted peak velocities with a median velocity of -423 km s^{-1} seen in Sombrero and -186 km s^{-1} in NGC 1052.

3. The highest-S/N ionic lines in Sombrero with show a clear blue wing extending >1000 km s^{-1} from the peak emission.

4. Sombrero has the lowest-luminosity high-IP lines ([O IV] and [Ne V]) yet detected in any source. NGC 1052 also shows low luminosity in both these lines, and the relative luminosity of these lines follows the relation seen in more luminous AGNs.

5. [Ne V] 14.32 μm is weak relative to [Ne II] 12.81 μm and [Ne III] 15.56 μm as compared to previously measured AGNs. This does not appear to be due to galaxy contamination, and thus likely indicates a deficiency of high-energy ionizing photons in these LLAGNs.

Our full ReveaLLAGN data set will include observations of seven nearby LLAGNs with both the NIRSpec IFU and MIRI/MRS. We will present the nuclear spectra of these in an upcoming paper (A. Seth et al., 2024, in preparation), as well as an analysis of their emission lines (K. Goold et al. 2024, in preparation). We will also be modeling the continuum emission and emission lines from the ReveaLLAGN sample (J. A. Fernández-Ontiveros et al. 2024, in preparation). The ReveaL-LAGN spectra will be valuable in both identifying the unique features of LLAGNs, and revealing the nature of the central engines in LLAGNs.

ORCID iDs

Kameron Goold ● https://orcid.org/0000-0002-7743-9906
Anil Seth ● https://orcid.org/0000-0003-0248-5470
Mallory Molina ● https://orcid.org/0000-0001-8440-3613
David Ohlson ● https://orcid.org/0009-0004-9457-2495
Jessie C. Runnoe ● https://orcid.org/0000-0001-8557-2822
Torsten Böker ● https://orcid.org/0000-0002-5666-7782
Timothy A. Davis ● https://orcid.org/0000-0003-4932-9379
Antoine Dumont ● https://orcid.org/0000-0003-0234-3376
Michael Eracleous ● https://orcid.org/0000-0002-3719-940X
Juan Antonio Fernández-Ontiveros ● https://orcid.org/0000-0001-9490-899X
Elena Gallo ● https://orcid.org/0000-0001-5802-6041
Andy D. Goulding ● https://orcid.org/0000-0003-4700-663X
Jenny E. Greene ● https://orcid.org/0000-0002-5612-3427
Luis C. Ho ● https://orcid.org/0000-0001-6947-5846
Sera B. Markoff ● https://orcid.org/0000-0001-9564-0876
Nadine Neumayer ● https://orcid.org/0000-0002-6922-2598
Richard M. Plotkin ● https://orcid.org/0000-0002-7092-0326
Almudena Prieto ● https://orcid.org/0000-0002-3585-2639
Shobita Satyapal ● https://orcid.org/0000-0003-2277-2354
Glenn van de Ven ● https://orcid.org/0000-0003-4546-7731
Jonelle L. Walsh ● https://orcid.org/0000-0002-1881-5908
Feng Yuan ● https://orcid.org/0000-0003-3564-6437
Anja Feldmeier-Krause ● https://orcid.org/0000-0002-0160-7221
Kayhan Gültekin ● https://orcid.org/0000-0002-1146-0198
Sebastian Hönig ● https://orcid.org/0000-0002-6353-1111
Allison Kirkpatrick ● https://orcid.org/0000-0002-1306-1545
Nora Lützgendorf ● https://orcid.org/0000-0002-4034-0080
Amy E. Reines ● https://orcid.org/0000-0001-7158-614X
Jay Strader ● https://orcid.org/0000-0002-1468-9668
Jonathan R. Trump ● https://orcid.org/0000-0002-1410-0470
Karina T. Voggel ● https://orcid.org/0000-0001-6215-0950

References

Appenzeller, I., & Oestreicher, R. 1988, AJ, 95, 45
Argyriou, I., Glasse, A., Law, D. R., et al. 2023, A&A, 675, A111
Armus, L., Lai, T. U. V., et al. 2023, ApJL, 942, L37
Asmus, D., Gandhi, P., Hönig, S. F., Smette, A., & Duschl, W. J. 2015, MNRAS, 454, 766
Asmus, D., Hoenig, S. F., Gandhi, P., Smette, A., & Duschl, W. J. 2014, MNRAS, 439, 1648
Astropy Collaboration, Price-Whelan, A. M., Sipőcz, B. M., et al. 2018, AJ, 156, 123
Blandford, R. D., & Begelman, M. C. 1999, MNRAS, 303, L1
Bushouse, H., Eisenhamer, J., Dencheva, N., et al. 2022, JWST Calibration Pipeline, v1.8.2, Zenodo,10.5281/zenodo.7229890
Cazzoli, S., Hermosa Muñoz, L., Márquez, I., et al. 2022, A&A, 664, A135
Chary, R., Becklin, E. E., Evans, A. S., et al. 2000, ApJ, 531, 756
Cheung, E., Bundy, K., Cappellari, M., et al. 2016, Natur, 533, 504
Claussen, M. J., Diamond, P. J., Braatz, J. A., Wilson, A. S., & Henkel, C. 1998, ApJL, 500, L129
Croton, D. J., Springel, V., White, S. D. M., et al. 2006, MNRAS, 365, 11
Dahmer-Hahn, L. G., Riffel, R., Ricci, T. V., et al. 2019, MNRAS, 489, 5653
Davé, R., Anglés-Alcázar, D., Narayanan, D., et al. 2019, MNRAS, 486, 2827
de Vaucouleurs, G., de Vaucouleurs, A., Corwin, H. G. J., et al. 1991, Third Reference Catalogue of Bright Galaxies (New York: Springer)
Dopita, M. A., Ho, I. T., Dressel, L. L., et al. 2015, ApJ, 801, 42
Dudik, R. P., Satyapal, S., Gliozzi, M., & Sambruna, R. M. 2005, ApJ, 620, 113
Elitzur, M., & Ho, L. C. 2009, ApJL, 701, L91
Elitzur, M., Ho, L. C., & Trump, J. R. 2014, MNRAS, 438, 3340
Emsellem, E., & Ferruit, P. 2000, A&A, 357, 111
Eracleous, M., Hwang, J. A., & Flohic, H. M. L. G. 2010, ApJS, 187, 135
Erkens, U., Appenzeller, I., & Wagner, S. 1997, A&A, 323, 707
Eskew, M., Zaritsky, D., & Meidt, S. 2012, AJ, 143, 139
Fabbiano, G., & Juda, J. Z. 1997, ApJ, 476, 666
Fender, R., & Belloni, T. 2004, ARA&A, 42, 317
Fernández-Ontiveros, J. A., López-Gonzaga, N., Prieto, M. A., et al. 2019, MNRAS, 485, 5377
Fernández-Ontiveros, J. A., López-López, X., & Prieto, A. 2023, A&A, 670, A22

Fernández-Ontiveros, J. A., Prieto, M. A., Acosta-Pulido, J. A., & Montes, M. 2012, JPhCS, 372, 012006

Fernández-Ontiveros, J. A., Spinoglio, L., Pereira-Santaella, M., et al. 2016, ApJS, 226, 19

Filho, M. E., Barthel, P. D., & Ho, L. C. 2006, A&A, 451, 71

Filippenko, A. V. 1985, ApJ, 289, 475

Filippenko, A. V., & Halpern, J. P. 1984, ApJ, 285, 458

Filippenko, A. V., & Sargent, W. L. W. 1988, ApJ, 324, 134

Flohic, H. M. L. G., Eracleous, M., Chartas, G., Shields, J. C., & Moran, E. C. 2006, ApJ, 647, 140

Fouque, P., Durand, N., Bottinelli, L., Gouguenheim, L., & Paturel, G. 1992, Catalogue of Optical Radial Velocities (Lyon: Observatoire de Lyon)

Gaia Collaboration, Brown, A. G. A., Vallenari, A., et al. 2021, A&A, 649, A1

Gallimore, J. F., Axon, D. J., O'Dea, C. P., Baum, S. A., & Pedlar, A. 2006, AJ, 132, 546

Gasman, D., Argyriou, I., Sloan, G. C., et al. 2023, A&A, 673, A102

González-Martín, O., Masegosa, J., Márquez, I., Guerrero, M. A., & Dultzin-Hacyan, D. 2006, A&A, 460, 45

González-Martín, O., Masegosa, J., Márquez, I., & Guainazzi, M. 2009, ApJ, 704, 1570

Goulding, A. D., & Alexander, D. M. 2009, MNRAS, 398, 1165

Greene, J. E., Ho, L. C., & Ulvestad, J. S. 2006, ApJ, 636, 56

Guainazzi, M., & Antonelli, L. A. 1999, MNRAS, 304, L15

Hada, K., Doi, A., Nagai, H., et al. 2013, ApJ, 779, 6

Heckman, T. M. 1980, A&A, 87, 152

Hermosa Muñoz, L., Cazzoli, S., Márquez, I., & Masegosa, J. 2020, A&A, 635, A50

Hernández-García, L., González-Martín, O., Márquez, I., & Masegosa, J. 2013, A&A, 556, A47

Hernández-García, L., González-Martín, O., Masegosa, J., & Márquez, I. 2014, A&A, 569, A26

Ho, L. C. 1999, ApJ, 516, 672

Ho, L. C. 2002, ApJ, 564, 120

Ho, L. C. 2008, ARA&A, 46, 475

Ho, L. C. 2009, ApJ, 699, 626

Ho, L. C., Filippenko, A. V., & Sargent, W. L. W. 1996, ApJ, 462, 183

Ho, L. C., Filippenko, A. V., & Sargent, W. L. W. 1997, ApJS, 112, 315

Ho, L. C., Greene, J. E., Filippenko, A. V., & Sargent, W. L. W. 2009, ApJS, 183, 1

Jardel, J. R., Gebhardt, K., Shen, J., et al. 2011, ApJ, 739, 21

Kadler, M., Kerp, J., Ros, E., et al. 2004a, A&A, 420, 467

Kadler, M., Ros, E., Lobanov, A. P., Falcke, H., & Zensus, J. A. 2004b, A&A, 426, 481

Kameno, S., Sawada-Satoh, S., Impellizzeri, C. M. V., et al. 2020, ApJ, 895, 73

Kennicutt, R. C. J., Armus, L., Bendo, G., et al. 2003, PASP, 115, 928

Kewley, L. J., Groves, B., Kauffmann, G., & Heckman, T. 2006, MNRAS, 372, 961

Komossa, S., Xu, D., Zhou, H., Storchi-Bergmann, T., & Binette, L. 2008, ApJ, 680, 926

Korista, K. T., & Ferland, G. J. 1989, ApJ, 343, 678

Koss, M. J., Ricci, C., Trakhtenbrot, B., et al. 2022, ApJS, 261, 2

Lambert, S. B., & Gontier, A. M. 2009, A&A, 493, 317

Li, Z., Jones, C., Forman, W. R., et al. 2011, ApJ, 730, 84

Maoz, D., Nagar, N. M., Falcke, H., & Wilson, A. S. 2005, ApJ, 625, 699

Marscher, A. P., & Gear, W. K. 1985, ApJ, 298, 114

Mason, R. E., Rodríguez-Ardila, A., Martins, L., et al. 2015, ApJS, 217, 13

McQuinn, K. B. W., Skillman, E. D., Dolphin, A. E., Berg, D., & Kennicutt, R. 2016, AJ, 152, 144

Meena, B., Crenshaw, D. M., Schmitt, H. R., et al. 2023, ApJ, 943, 98

Meenakshi, M., Mukherjee, D., Wagner, A. Y., et al. 2022, MNRAS, 516, 766

Meier, D. L. 2001, ApJL, 548, L9

Meléndez, M., Kraemer, S. B., & Schmitt, H. R. 2010, MNRAS, 406, 493

Mezcua, M., & Prieto, M. A. 2014, ApJ, 787, 62

Molina, M., Eracleous, M., Barth, A. J., et al. 2018, ApJ, 864, 90

Müller-Sánchez, F., Prieto, M. A., Hicks, E. K. S., et al. 2011, ApJ, 739, 69

Müller-Sánchez, F., Prieto, M. A., Mezcua, M., et al. 2013, ApJL, 763, L1

Nagar, N. M., Falcke, H., Wilson, A. S., & Ulvestad, J. S. 2002, A&A, 392, 53

Nagar, N. M., Falcke, H., & Wilson, A. S. 2005, A&A, 435, 521

Narayan, R., & Yi, I. 1995, ApJ, 452, 710

Nemmen, R. S., Storchi-Bergmann, T., & Eracleous, M. 2014, MNRAS, 438, 2804

Nicastro, F., Martocchia, A., & Matt, G. 2003, ApJL, 589, L13

Nussbaumer, H., & Osterbrock, D. E. 1970, ApJ, 161, 811

Oliva, E., Salvati, M., Moorwood, A. F. M., & Marconi, A. 1994, A&A, 288, 457

Panessa, F., Barcons, X., Bassani, L., et al. 2007, A&A, 467, 519

Park, J., Hada, K., Kino, M., et al. 2019, ApJ, 871, 257

Pellegrini, S., Baldi, A., Fabbiano, G., & Kim, D. W. 2003, ApJ, 597, 175

Pellegrini, S., Fabbiano, G., Fiore, F., Trinchieri, G., & Antonelli, A. 2002, A&A, 383, 1

Pereira-Santaella, M., Álvarez-Márquez, J., García-Bernete, I., et al. 2022, A&A, 665, L11

Pier, E. A., & Voit, G. M. 1995, ApJ, 450, 628

Plotkin, R. M., Anderson, S. F., Brandt, W. N., et al. 2012, ApJL, 745, L27

Pogge, R. W., Maoz, D., Ho, L. C., & Eracleous, M. 2000, ApJ, 532, 323

Pontoppidan, K. M., Barrientes, J., Blome, C., et al. 2022, ApJL, 936, L14

Porth, O., Chatterjee, K., Narayan, R., et al. 2019, ApJS, 243, 26

Prieto, M. A., Fernández-Ontiveros, J. A., Markoff, S., Espada, D., & González-Martín, O. 2016, MNRAS, 457, 3801

Prieto, M. A., Mezcua, M., Fernández-Ontiveros, J. A., & Schartmann, M. 2014, MNRAS, 442, 2145

Prieto, M. A., Nadolny, J., Fernández-Ontiveros, J. A., & Mezcua, M. 2021, MNRAS, 506, 562

Prieto, M. A., Reunanen, J., Tristram, K. R. W., et al. 2010, MNRAS, 402, 724

Ricci, C., Trakhtenbrot, B., Koss, M. J., et al. 2017, ApJS, 233, 17

Rodríguez-Ardila, A., Prieto, M. A., Portilla, J. G., & Tejeiro, J. M. 2011, ApJ, 743, 100

Rodríguez-Ardila, A., Prieto, M. A., Viegas, S., & Gruenwald, R. 2006, ApJ, 653, 1098

Sajina, A., Lacy, M., & Pope, A. 2022, Univ, 8, 356

Satyapal, S., Vega, D., Dudik, R. P., Abel, N. P., & Heckman, T. 2008, ApJ, 677, 926

Sheth, K., Regan, M., Hinz, J. L., et al. 2010, PASP, 122, 1397

Shi, F., Li, Z., Yuan, F., & Zhu, B. 2021, NatAs, 5, 928

Sikora, M., Stawarz, Ł., & Lasota, J.-P. 2007, ApJ, 658, 815

Silk, J., & Rees, M. J. 1998, A&A, 331, L1

Stern, J., Laor, A., & Baskin, A. 2014, MNRAS, 438, 901

Sugai, H., Hattori, T., Kawai, A., et al. 2005, ApJ, 629, 131

Terashima, Y., & Wilson, A. S. 2003, ApJ, 583, 145

Tommasin, S., Spinoglio, L., Malkan, M. A., & Fazio, G. 2010, ApJ, 709, 1257

Tonry, J. L., Dressler, A., Blakeslee, J. P., et al. 2001, ApJ, 546, 681

Trump, J. R., Impey, C. D., Kelly, B. C., et al. 2011, ApJ, 733, 60

Walsh, J. L., Barth, A. J., Ho, L. C., et al. 2008, AJ, 136, 1677

Wang, Q. D., Nowak, M. A., Markoff, S. B., et al. 2013, Sci, 341, 981

Weinberger, R., Springel, V., Hernquist, L., et al. 2017, MNRAS, 465, 3291

Wells, M., Pel, J. W., Glasse, A., et al. 2015, PASP, 127, 646

Wilson, A. S., & Raymond, J. C. 1999, ApJL, 513, L115

Wrobel, J. M. 1984, ApJ, 284, 531

Xue, Y. Q., Luo, B., Brandt, W. N., et al. 2016, ApJS, 224, 15

Yuan, F., Bu, D., & Wu, M. 2012, ApJ, 761, 130

Yuan, F., Gan, Z., Narayan, R., et al. 2015, ApJ, 804, 101

Yuan, F., & Narayan, R. 2014, ARA&A, 52, 529